On the design of compact hydraulic pipe flocculators using CFD-PBE

Bilde, Kasper Gram; Hærvig, Jakob; Sørensen, Kim

Published in:
Chemical Engineering Research & Design

DOI (link to publication from Publisher):
10.1016/j.cherd.2023.04.045

Publication date:
2023

Document Version
Publisher's PDF, also known as Version of record

Available online at www.sciencedirect.com

Chemical Engineering Research and Design

journal homepage: www.elsevier.com/locate/cherd

On the design of compact hydraulic pipe flocculators using CFD-PBE

Kasper Gram Bilde[a,b,*], Jakob Hærvig[a], Kim Sørensen[a]

[a] Aalborg University, AAU Energy, Pontoppidansstræde 111, Aalborg 9220, Denmark
[b] Alfa Laval Aalborg A/S, Gasværksvej 21, Aalborg 9000, Denmark

ARTICLE INFO

Article history:
Received 31 August 2022
Received in revised form 16 March 2023
Accepted 19 April 2023
Available online 24 April 2023

Keywords:
Multiphase flow
Particle aggregation
Particle breakage
Population balance equation
CFD-PBE

ABSTRACT

Designing a compact hydraulic pipe flocculator is a common challenge for various water purification and wastewater processes where space is limited. Various geometrical parameters are analysed to identify the most important parameters when designing an efficient system for a Reynolds number of Re_D = 20, 000. A coupled CFD-PBE model is applied to a total of 123 geometrical configurations to simulate particle aggregation and breakage due to the local velocity gradients in the configurations. The shear present in the 90° pipe bends is the dominating factor in the final aggregate size and therefore the most important geometrical factor is the bend radius. Secondly, it is observed that the primary length, L_1, has the second-largest impact as a linearly increasing particle diameter is observed along the straight pipe. Helically coiled geometrical configurations with no straight sections, $L_1 = L_2 = 0$, and a bend radius of $r_b \geq 2d_h$ result in large particles as a constant but moderate cross-sectionally averaged turbulent energy dissipation is observed throughout the pipe. The largest volume-averaged particle size is observed for a configuration with a primary length of $L_1 = 20d_h$, a secondary length of $L_2 = 0$ and a bend radius of $r_b = 2.5d_h$.

1. Introduction

Flocculation of micron-sized particles is an important operation for a large range of freshwater and wastewater treatment plants to achieve an efficient liquid-solid separation. As many wastewater treatment plants rely on the separation of solids due to sedimentation it is important to obtain large stable agglomerates, as the sedimentation velocity, v_s, is a function of the effective particle diameter, $v_s \propto d_p^2$ according to Stokes law of settling.

Flocculation systems can generally be categorised into two groups, namely mechanical- and hydraulic flocculation. In mechanical flocculation systems, a mechanical stirrer is operated to introduce sufficient magnitudes of velocity fluctuations in the fluid which causes the particles to collide and agglomerate. The turbulence in hydraulic flocculation systems is driven by the fluid flow as the fluid passes through the application which introduces velocity fluctuations, e.g. a baffled basin, where the velocity fluctuations in the flow are driven by flow obstructions caused by the baffles. In land-based wastewater treatment systems, baffled basins with a large surface area, often referred to as the footprint, are often used, but some industries do not have the space for such large basins or tanks. This is the case for marine water treatment plants, where a compact pipe flocculator can be utilised, which consists of a series of consecutive circular pipe bends.

* Corresponding author at: Aalborg University, AAU Energy, Pontoppidansstræde 111, Aalborg 9220, Denmark.
E-mail address: kgb@energy.aau.dk (K.G. Bilde).

https://doi.org/10.1016/j.cherd.2023.04.045

Nomenclature

A	area (m^2)
a	aggregation frequency
B	strength parameter (m^3/s^3)
b	breakage frequency
C	coefficient (-)
d	diameter (m)
D_f	fractal dimension (-)
F	force (N)
f	fraction
g	gravitational acceleration (m/s^2)
k	turbulent kinetic energy (m^2/s^2)
L	length (m)
M	interfacial momentum transfer
$\dot{m}$	mass flow (kg/s)
n	number (-)
p	pressure (Pa)
r	radius (m)
Re	Reynolds number ($\|u\| d_h/\nu$)
S	source term
Sc	Schmidt number (-)
t	time (s)
u	velocity (m/s)
v	volume (m^3)

Greek letters

α	volume fraction (-)
β	daughter size distribution function
ε	turbulent energy dissipation rate (m^2/s^3)
μ	dynamic viscosity (Pa s)
ν	kinematic viscosity (m^2/s)
ρ	density (kg/m^3)
σ	turbulent Schmidt number (-)
τ	stress tensor (N/m^2)
ω	vorticity ($\nabla \times \boldsymbol{u}$)

Subscripts

0	primary particle
32	Sauter mean
φ	phase
b	bend
cr	critical rate
D	drag
f	fluid
h	hydraulic
L	lift
p	particle
T	turbulent dispersion
VM	virtual mass

Historically, Smoluchowski (1917) formulated a mathematical model describing the theoretical orthokinetic flocculation of particles under laminar conditions. In practice, flocculation happens under turbulent conditions, which is why Camp and Stein (1943) replaced the velocity gradient term, du/dz with a measurable average value using the root mean square (RMS) velocity gradient. The RMS velocity gradient then becomes a function of the total power dissipated in the entire system. In more recent years, computational fluid dynamics (CFD) has proven to be a reliable method to describe the local energy dissipation within a system and several researchers have shown the capabilities of using CFD to predict orthokinetic flocculation in both mechanical and hydraulic systems (Bridgeman, 2006; Vadasarukkai et al., 2011; Törnblom, 2018; Oliveira and Donadel, 2019; Zhan et al., 2021).

Laine et al. (1999) were among the early researchers to use CFD to study the settling of particles in a flocculation tank. Three different regimes were determined inside the settling tank, namely rapid agitation, slow agitation and laminar flow. The turbulence in the flow was modelled using the Re-Normalisation Group (RNG) k-ε model proposed by Yakhot et al. (1992) and from the velocity contours the researchers concluded that the fluid motion sometimes caused aggregates to flow to the surface and thereby float instead of sink.

Bridgeman et al. (2008) used CFD to study the local velocity gradient with a focus on particle agglomeration and breakage. The authors studied the local velocity gradient using a single-phase steady-state Reynolds-averaged Navier Stokes (RANS) model to simulate the shear introduced by a mechanical stirrer in a flocculation tank. The experimental- and numerical data obtained were in good agreement and expressions for the strength and breakage of an aggregate as a function of the local velocity gradient were presented.

Several researchers have applied the single-phase RANS modelling approach to simulate the hydraulics within a flocculation system with the focus on describing the local velocity gradient (Bridgeman et al., 2010; Sartori et al., 2015; Gar Alalm et al., 2016; Xiang et al., 2018; Oliveira and Donadel, 2019). The referred studies have shown that a local large velocity gradient is found inside the hydraulic domain, which leads to a local zone where the agglomerates are highly prone to breakage.

In more recent years, researchers have simulated the agglomeration and breakage of agglomerates using multi-phase CFD. Focusing on a small 2-dimensional domain, Qiu et al. (2016) described the agglomeration and sedimentation of spherical particles using a coupling of CFD and discrete element modelling (DEM) using the Johnson-Kendall-Roberts adhesion theory. The researchers showed how agglomerated particles within lid-driven cavity sediments sink as opposed to small non-agglomerated particles.

The CFD-DEM models have high predicting capabilities as collisions between particles are resolved, but due to their nature of resolving each Lagrangian particle, this limits the use within flocculation systems as particles are usually within the micron-sized range. For industrial applications, this means that the number of Lagrangian particles quickly exceeds $n_p > 10^{12}$ making it unfeasible even with modern computing capacities. Therefore, coarse-graining of the particles is often used (Tausendschön et al., 2020; Jiang et al., 2020), or alternative, other methods are applied to solve the particle phase and the momentum exchange between the phases.

Another approach, which has been applied successfully, is to use the coupled population balance equation (PBE) to track the number density function of the disperse phase within the computational domain (Marchisio et al., 2003; Yao et al., 2014a,b; Lau and Kind, 2016; Wang et al., 2022). Different solutions of the PBE have been applied throughout the literature, but the majority of the papers from recent years are based on the methods of moments (MOM) and its derivatives. Marchisio et al. (2003) applied the quadrature MOM (QMOM) to solve the PBE and describe the aggregation and breakage of solid particles in a Taylor-Couette flow. As the

QMOM is based on solving a consecutive set of low-order integer moments of the number density function, the integral source terms of the PBE are approximated using Gaussian quadrature. To solve for a continuous number density function, Yuan et al. (2012) proposed the Extended QMOM (EQMOM) and Passalacqua et al. (2018) implemented this approach as the OpenQBMM module for the OpenFOAM CFD library. Kumar and Ramkrishna (1996) proposed another solution to the PBE by discretising the PBE into several classes, which is why this method is often referred to as the class method or sometimes also the discrete- or sectional method. Lehnigk et al. (2021) implemented the class method into the OpenFOAM CFD library as part of the Euler-Euler model and used it to successfully simulate the synthesis of titania powder in a tubular reactor. The QMOM requires a low number of scalar equations, making this method the least computationally expensive, but this method has the drawback that there is no direct information about the number density function and its shape. The EQMOM provides this additional information as the number density function is approximated using a combination of kernel density functions. The EQMOM is, however, more computationally expensive compared to the QMOM and Li et al. (2017) reports that the EQMOM is up to 30x more computationally expensive than the QMOM. The class method is also more computationally expensive than the QMOM, as a set of discrete PBE has to be solved for each size class, and this method also requires some knowledge of the particle size range in advance. The advantage of the class method is that the number density function and its shape are readily available at any point and time in the computational domain. This also means that this method is highly intuitive to apply, as knowledge of the particle size range is often known and the shape of the number density function is often the parameter of interest.

In this study, the geometrical parameters of a hydraulic pipe flocculator are varied to analyse the effects on the particle size distribution. The geometrical parameters are the primary length, L_1, the secondary length, L_2, the bend radius r_b and the pitch of inclination, φ. The geometrical parameters are shown in Fig. 1. The parameters are varied as a function of the hydraulic diameter of the pipe, d_h.

2. Numerical framework

All geometrical configurations presented in this study are constructed with the same cross-sectional mesh, which is seen in Fig. 1. The computational mesh is made of hexahedral cells with a maximum angle of 120°.

2.1. Governing equations

The multiphase flow is described by the governing equations in the Euler-Euler framework, where a set of continuity and momentum equations is solved for each phase, φ. The fluid- and particle phases are assumed incompressible and isothermal, resulting in the governing equations seen in Eqs. (1) and (2).

$$\frac{\partial}{\partial t}(\alpha_\varphi \rho_\varphi) + \nabla\cdot(\alpha_\varphi \rho_\varphi \boldsymbol{u}_\varphi) = 0 \tag{1}$$

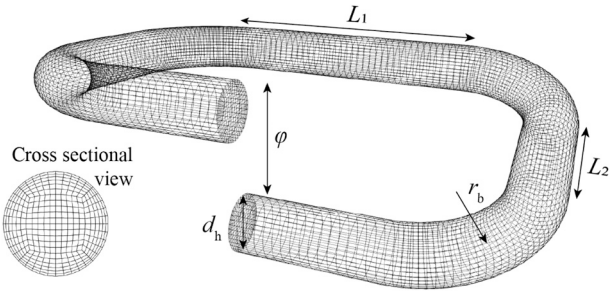

Fig. 1 – The geometrical configuration of the setup. The pitch of inclination, φ, denotes the height between each pass, the primary and secondary lengths, L_1 and L_2, denote the length in the primary and secondary direction and the bend radius of the pipe is denoted by r_b.

$$\frac{\partial}{\partial t}(\alpha_\varphi \rho_\varphi \boldsymbol{u}_\varphi) + \nabla\cdot(\alpha_\varphi \rho_\varphi \boldsymbol{u}_\varphi \boldsymbol{u}_\varphi) - \nabla\cdot\tau_\varphi = -\alpha_\varphi \nabla p + \alpha_\varphi \rho_\varphi \boldsymbol{g} + \boldsymbol{M}_\varphi + \boldsymbol{S}_\varphi, \tag{2}$$

where α is the volume fraction, ρ is the density, $\boldsymbol{u}$ is the velocity, τ is the stress tensor, p is the pressure which is shared by the continuous- and dispersed phase, $\boldsymbol{g}$ is the gravitational acceleration, $\boldsymbol{S}$ is the momentum source term. $\boldsymbol{M}$ is the momentum exchange at the interface between the phases which is defined as

$$\boldsymbol{M}_\varphi = \sum_{\varphi=0,\varphi\neq\xi}^{N} (\boldsymbol{F}_{L,\varphi\xi} + \boldsymbol{F}_{D,\varphi\xi} + \boldsymbol{F}_{T,\varphi\xi} + \boldsymbol{F}_{VM,\varphi\xi}), \tag{3}$$

where $\boldsymbol{F}_L$ is the lift force, $\boldsymbol{F}_D$, is the drag force, $\boldsymbol{F}_T$ is the turbulent dispersion force and $\boldsymbol{F}_{VM}$ is the virtual mass force transferred between phase φ and ξ. As momentum is conserved, it is implied that $\sum_\varphi \boldsymbol{M}_\varphi = 0$. A source term is added in the continuous phase to maintain a desired velocity by adding a pressure gradient increment to the pressure gradient in Eq. (2) to maintain the desired bulk velocity. The governing equations are solved using the Reynolds averaged Navier Stokes (RANS) model, where the averaged components are solved and the fluctuating components are modelled.

2.2. Continuous phase turbulence modelling

To account for turbulence in the continuous phase, the stress tensor, τ_f, is modelled using the Re-Normalisation Group k-ε model by Yakhot et al. (1992). The statistical Re-Normalisation group theory is applied to resolve the smallest eddies in the inertial range. This procedure effectively removes small scales of turbulence by modifying the turbulent viscosity. The two-equation RNG k-ε provides the closure equations for modelling the turbulence. The governing equations for the RNG k-ε are given by

$$\frac{\partial}{\partial t}(\alpha_f \rho_f k) + \nabla\cdot(\alpha_f \rho_f k \boldsymbol{u}_f) = \nabla\left[\left(\mu_f + \frac{\mu_t}{\sigma_k}\right)\nabla k\right] + P_k - \alpha_f \rho_f \varepsilon \tag{4}$$

and

$$\frac{\partial}{\partial t}(\alpha_f \rho \varepsilon) + \nabla\cdot(\alpha_f \rho_f \varepsilon \boldsymbol{u}_f) = \nabla\left[\left(\mu_f + \frac{\mu_t}{\sigma_\varepsilon}\right)\nabla \varepsilon\right] + C_{1\varepsilon}\frac{\varepsilon}{k}P_k - C_{2\varepsilon}\alpha_f \rho \frac{\varepsilon^2}{k}, \tag{5}$$

where P_k is the production of turbulence due to the mean velocity gradients. In this work, the default values of coefficients $C_{1\varepsilon} = 1.42$ and $C_{2\varepsilon} = 1.68$ are applied.

Escue and Cui (2010) compared the higher-order Reynolds stress turbulence model (RSM) and the lower-order RNG k-ε model to experimental data for swirling flow in a pipe and concluded that the RNG k-ε was superior to the RSM model for low swirling flows. Reasonable predictions of the high swirling flows were obtained using the RNG k-ε model. Due to its comparatively low computational cost and high accuracy in predicting turbulence in swirling flows, the RNG k-ε is chosen in this study.

2.3. Dispersed phase pressure

In this study no shear stress tensor is applied for the particle phase, as the volume fraction is low, meaning that particle-particle interactions are neglected in this study. As a non-physical, high packing density in the smallest cells is still possible, even with low bulk volume fractions, an exponential phase pressure model is applied to the particle phase. This particle phase pressure increases exponentially when the particle volume fraction approaches a maximum packing density, thereby preventing the particle phase from exceeding the maximum packing density, $\alpha_{p,max}$. A pressure gradient concerning the volume fraction is added to the momentum equation, as given by

$$p' = g_0 \cdot \min\left[\exp\left(\alpha_{p,exp}(\alpha_p - \alpha_{p,max})\right), \frac{p'}{max}\right], \tag{6}$$

where a maximum allowable packing density of $\alpha_{p,max} = 0.62$ is applied along with the default values of $g_0 = 1000$, $\alpha_{p,exp} = 500$ and $p'_{max} = 1000$.

2.4. Lift force

To account for the lift force generated by the swirling flow around the aggregates, a lift force is applied

$$\mathbf{F}_L = -C_L \rho_f \alpha_p \mathbf{u}_r \cdot \boldsymbol{\omega}, \tag{7}$$

where the $\boldsymbol{\omega}$ is the vorticity of the continuous phase defined by $\boldsymbol{\omega} = \nabla \times \mathbf{u}_f$. The lift force coefficient, C_L, of Saffman (1965) and later modified and extended for finite Reynolds numbers by Mei (1992) is applied. The lift force coefficient is given as

$$C_L = \frac{3}{2\pi\sqrt{Re_\omega}} C'_L \tag{8}$$

where the modified lift force coefficient, C'_L, is defined as

$$C'_L = \begin{cases} 6.46[(1 - 0.3314\beta^{0.5})e^{-0.1Re_p} + 0.3314\beta^{0.5}] & Re_p \le 40 \\ 6.46 \cdot 0.0524\sqrt{\beta Re_p} & Re_p > 40. \end{cases} \tag{9}$$

Herein, Re_ω is the vorticity Reynolds number which is defined as $Re_\omega = |\boldsymbol{\omega}| d_p^2/\nu_f$, Re_p is the particle Reynolds number, defined as $Re_p = |\mathbf{u}_p - \mathbf{u}_f| d_p/\nu_f$ and $\beta = 0.5(Re_\omega/Re_p)$.

2.5. Drag force

The drag force acting on the particle phase by the fluid phase is the dominating interfacial momentum transfer term and is described by

$$\mathbf{F}_D = \frac{1}{2}\rho_f |\mathbf{u}_r| \mathbf{u}_r C_D A_p, \tag{10}$$

where A_p is the projected surface area of the aggregates and C_D is the drag force coefficient. The drag force coefficient model of Wen and Yu (1966) is applied in this study and is given as

$$C_D = \begin{cases} \frac{24}{Re_p}\alpha_f^{-2.65} & \text{for } Re_p < 0.5 \\ \frac{24}{Re_p}(1 + 0.15Re_p^{0.687})\alpha_f^{-2.65} & \text{for } 0.5 \le Re_p < 1000 \\ 0.44\alpha_f^{-2.65} & \text{for } Re_p \ge 1000. \end{cases} \tag{11}$$

The drag coefficient model is applicable for spherical particles meaning the particles are assumed to be spherical. This is a simplification of shape of the particles, as they are fractal-like in their nature. Mikhailov et al. (2006) analysed the optical properties of soot using an experimental technique and concluded that soot fractals form a compact shape close to a sphere when the soot particles are subject to a wet environment. Fan et al. (2016) showed how soot particles age from a loosely coupled fractal to a strongly coupled fractal when subject to a wet environment. As the particles in this study are soot and are suspended in water, this justifies the assumption of spherical particles.

2.6. Turbulent dispersion force

As the Stokes number of the particles is small, $St = t_0 u_p/l_0 < 1$, they follow the streamlines of the flow. This also means that the particles tend to follow the velocity fluctuations of the continuous phase and as the turbulence is modelled using a k-ε model, the velocity fluctuations are only modelled. As the continuous phase is modelled using RANS, only the mean velocity is resolved. To account for velocity fluctuations of the continuous phase, the turbulent dispersion force is included. Burns et al. (2004) performed Favre averaging of the drag force acting on the dispersed phase and proposed the turbulent dispersion force as

$$\mathbf{F}_{disp} = -\frac{3}{4}C_D \frac{\alpha_p \rho_f}{d_p} \mathbf{u}_r \frac{\nu_t}{Sc_t}\left(\frac{\nabla\alpha_f}{\alpha_f} - \frac{\nabla\alpha_p}{\alpha_p}\right), \tag{12}$$

where Sc_t is the turbulent Schmidt number, which is assumed $Sc_t = 0.9$ in this study.

2.7. Virtual mass force

When there is a relative acceleration between the dispersed and continuous phases, an additional force arises due to the acceleration of the fluid surrounding the particle. This virtual mass force is given by

$$\mathbf{F}_{VM} = -C_{VM}\rho_f \alpha_p \left(\frac{D_p}{Dt}\mathbf{u}_p - \frac{D_f}{Dt}\mathbf{u}_f\right), \tag{13}$$

where $C_{VM} = 0.5$ is the virtual mass force coefficient for spherical particles, D_p/Dt and D_f/Dt are the material derivatives of the dispersed and continuous phase, respectively.

2.8. Population balance equation

The temporal evolution of the particle size distribution is modelled using the population balance equation, which is a transport equation for the number density function. The number density function, $n(\xi, \mathbf{x}, t)$, is a function of an internal value ξ, a spatial coordinate, $\mathbf{x}$ at a given time, t. For many studies (Wang et al., 2019; Liao et al., 2018; Salehi et al., 2017), including this study, the internal value of interest is the particle size, which is why the particle volume is used as

the internal value, $\xi = v_p$. The population balance equation for the number density function is given as

$$\frac{\partial}{\partial t} n_v + \nabla \cdot (\boldsymbol{u}_p n_v) = S_v, \tag{14}$$

where the number density function as a function of the volume is denoted by n_v for the ease of notation and S_v is the source term accounting for the discontinuous changes in the number density function, e.g. aggregation and breakage. The source term of the PBE is given by

$$S_v = \frac{1}{2}\int_0^v n_{v'} n_{v-v'} a_{v',v-v'} \mathrm{d}v' - n_v \int_0^\infty n_{v'} a_{v,v'} \mathrm{d}v' + \int_v^\infty n_{v'} b_{v'} \beta_{v,v'} \mathrm{d}v' - n_v b_v, \tag{15}$$

where the two first terms on the right-hand side account for the changes due to aggregation and $a_{v,v'}$ is the aggregation frequency. The two last terms account for the changes due to breakage, where $b_{v'}$ is the breakage frequency and $\beta_{v,v'}$ is the daughter size distribution. For details on the algorithm and discretisation, the reader is referred to the work of Lehnigk et al. (2021) who describes how the class method is implemented into the OpenFOAM CFD library.

2.9. Breakage kernel

The breakage kernel by Kusters (1991) is applied in this study to account for the birth and death of particles due to breakage. The breakage frequency is modelled as an exponential function accounting for the maximum particle strength required for the particle to break, as given by

$$b_{v'} = \sqrt{\frac{4}{15\pi}} \sqrt{\frac{\varepsilon}{\nu}} \exp\left(-\frac{\varepsilon_{cr}}{\varepsilon}\right), \tag{16}$$

where ε_{cr} is the critical energy dissipation rate required for the aggregate to break, which is defined as

$$\varepsilon_{cr} = \frac{B}{r_c}, \tag{17}$$

where B is a parameter representing the inter-particle adhesive bond of the particles which accounts for the critical energy dissipation rate required for the particle to break and r_c is the collision radius. Mandelbrot (1985) proposed the correlation for the collision radius as

$$r_c = r_0 \left(\frac{n_i}{k_c}\right)^{1/D_f}, \tag{18}$$

where r_0 is the radius of the primary particles within an aggregate, n_i is the number of primary particles in the aggregate and k_c is a coefficient relative to packing and is assumed unity in this study (Jeldres et al., 2017). A constant fractal dimension, D_f is assumed when using this approach, meaning aggregates with a high fractal dimension withstand a higher energy dissipation rate compared to aggregates with a lower fractal dimension.

In a previous study, Bilde et al. (2022) showed a good agreement between an experimentally measured particle size distribution using a Malvern Mastersizer 3000 and the numerical particle size distribution obtained for a similar RANS model when using an aggregate strength parameter of $B = 50 \cdot 10^{-7}$ m^3/s^3.

2.10. Daughter size distribution

The discretised daughter size distribution suggested by Laakkonen et al. (2007) is implemented in this study. The daughter size distribution is a beta distribution describing the distribution of daughter particles as a function of the number of daughter particles and is given as

$$\beta_{v,v'} = (1 + C_4)(2 + C_4)(3 + C_4)(4 + C_4)\left(\frac{1}{3}\right)\left(\frac{1}{v'}\right)\left(\frac{v}{v'}\right)^2\left(1 - \frac{v}{v'}\right)^{C_4}, \tag{19}$$

where v and v' are the volumes of the daughter and mother particle, respectively, and C_4 is a coefficient describing the total number of daughters generated. The number of daughter particles is given by

$$n_i = \frac{4}{3} + \frac{C_4}{3}. \tag{20}$$

Bilde et al. (2022) showed good agreement between experimental and numerical particle size distributions when using a binary breakage coefficient of $C_4 = 2$.

2.11. Aggregation kernel

The aggregation kernel of Adachi et al. (1994) is applied in this study to account for the birth and death of new aggregates due to aggregation. This model describes the orthokinetic aggregation of particles in turbulent flows and the aggregation frequency is given by

$$a_{d,d'} = \frac{4}{3}\sqrt{\frac{3\pi}{10}} \sqrt{\frac{\varepsilon}{\nu}} (d + d')^3, \tag{21}$$

where d and d' denote the diameter of two colliding aggregates.

3. Numerical properties and initialisation

The results presented in the following section are time averaged values, where the value of interest is averaged over the dimensionless time of $t^+ = t\,u/d_h = 100$ after a steady-state solution has been obtained. The particle phase is initialised with a monodisperse particle size distribution where all particles are positioned in the smallest size group of $d_p = 1\mu$m. The fluid flow is initialised without the particle phase using a steady-state single-phase model until a converged flow is obtained and then the monodisperse particles are inserted into the fully-developed fluid velocity profile. A series of simulations are carried out for different geometrical configurations to study the impact of the different compact designs.

3.1. Geometrical configuration

To study the particle size distribution until a steady-state solution is obtained, periodic boundary conditions are applied to the geometrical configuration. This effectively creates an infinitely long pipe flocculator where the mass- and momentum transport leaving at the outlet is re-applied at the inlet. This approach decreases the number of computational cells in the domain and a converged steady-state solution is obtained faster.

The pitch of inclination, φ, the primary and secondary lengths, L_1 and L_2, as well as the bend radius, r_b, are the geometrical parameters of interest in this study and these

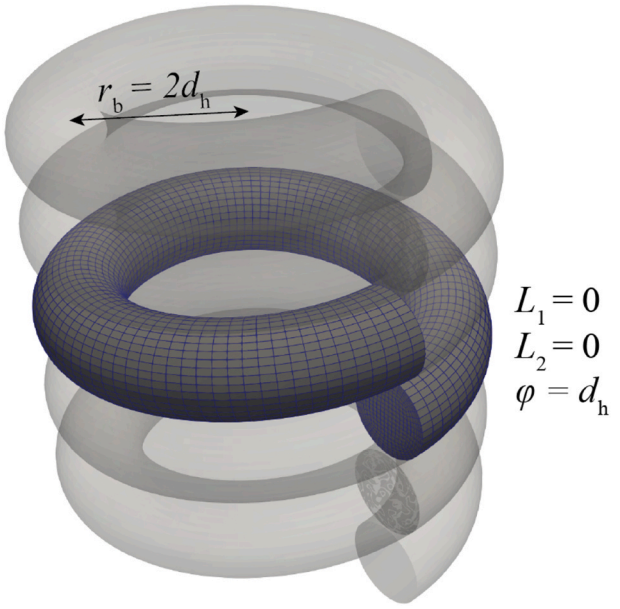

Fig. 2 – Example of a helical coiled tube flocculator with a bend radius of $r_b = 2d_h$, pitch inclination of $\varphi = d_h$ and primary and secondary lengths of $L_1 = L_2 = 0$.

are seen in Fig. 1. All the parameters of interest are scaled using the hydraulic diameter of the pipe, d_h.

The geometrical configuration allows for analysing the impact of various combinations including a helically coiled tube flocculator, as previously reported by Oliveira and Donadel (2019), when setting $L_1 = 0$ and $L_2 = 0$, as seen in Fig. 2.

In this study, the geometrical configurations are bounded by a set of values to limit the number of simulations carried out. In practice, this also means that the configuration is limited to a certain primary and secondary length, which makes out the footprint of the pipe flocculator. The primary length is bounded by $0 \leq L_1 \leq 20d_h$, the secondary length is bounded by $0 \leq L_2 \leq 10d_h$, the bend radius is bounded by $d_h \leq r_b \leq 2.5d_h$ and the pitch inclination is bounded by $d_h \leq \varphi \leq 3d_h$.

3.2. Simulation parameters

Particle properties from our previous study (Bilde et al., 2022) have been re-used in this study and can be seen in Table 1. The particles analysed resembles soot particles suspended in water in terms of physical- and chemical properties, where soot is assumed to mainly consist of graphite. In our previous study, these parameters were validated against an experimentally obtained particle size distribution and a mesh independent particle size distribution was presented when using a grid with a first cell height of $y^+_{min} = 30$ and a maximum cell height of $y^+_{max} = 70$ in the middle of the pipe. The particles size distribution is bounded by a minimum size of $d_{p,min} = 1\mu m$ and a maximum size of $d_{p,max} = 1000\mu m$. The particle size range is discretised into a total of 50 logarithmically spaced size classes with a spacing given by

$$\log_{10}\left(\frac{d_{p,i}}{d_{p,i-1}}\right) = \frac{\log_{10}\left(\frac{d_{p,N}}{d_{p,1}}\right)}{N-1} \qquad 1 < i < N. \tag{22}$$

Table 1 – Fluid- and particle properties applied for the CFD-PBE model.

Property	Symbol	Value	Unit
Daughter size coefficient	C_4	2	–
Fractal dimension	D_f	2.3	–
Kinematic viscosity	ν_f	10^{-6}	m^2/s
Particle density	ρ_p	1400	kg/m^3
Particle strength parameter	B	$50 \cdot 10^{-7}$	m^3/s^3
Primary particle size	d_0	250	nm

All simulations are carried out for a fluid flow with a turbulent Reynolds number of $Re_D = 20,000$, corresponding to a plug flow velocity of $\bar{u} = 0.5$ m/s.

4. Results and discussion

4.1. Inclination pitch

The impact of increasing the inclination pitch is analysed before analysing the other geometrical parameters, as this parameter is assumed to have a minor impact on the particle size distribution. A computational domain with a constant primary- and secondary length of $L_1 = 5d_h$ and $L_2 = 2d_h$ and a constant bend radius of $r_b = 2d_h$ is constructed. The pitch is bounded by $d_h \leq \varphi \leq 3d_h$ and varied by integer intervals, resulting in a total of 3 simulations.

The converged particle size distributions for the three simulations are seen in Fig. 3, where the volumetric density function is plotted as a function of the particle diameter. The difference between the simulations is negligible, meaning that the pitch has a negligible impact on the particle size distribution for the liquid-solid flow in this study when dealing with a pitch of inclination within the range of $d_h \leq \varphi \leq 3d_h$ and will be analysed no further in this study.

In practice, this observation means that there is no performance difference for a pipe flocculator with a smaller pitch, which is, in many cases more desirable, as the pipe flocculator takes up less volume and thereby becomes more compact.

4.2. Geometrical parameters

The effect of the three remaining parameters, namely the bend radius, r_b, the primary length, L_1 and the secondary length L_2, is analysed to study the particle size distribution. As the parameters are bounded, a total of 120 simulations are carried out, varying the bend radius with intervals of $0.5d_h$, the primary length by $5d_h$ and the secondary length by $2d_h$.

4.3. Particle size over the total length

The amount of turbulence induced within the pipe changes throughout the geometry depending on the given configuration and to visualise the impact of this, the area-average of the time-averaged Sauter mean diameter, $\bar{d}_{32}$, is used to visualise the changing particle size distribution over the length of the pipe. As the geometrical configuration is periodic around the centre of length, the area averaged Sauter mean diameter is also periodic, which is evident from Fig. 4 for 5 configurations. It is immediately visible that the Sauter mean diameter along the length of the pipe consists of some recognisable patterns for all configurations, except for the

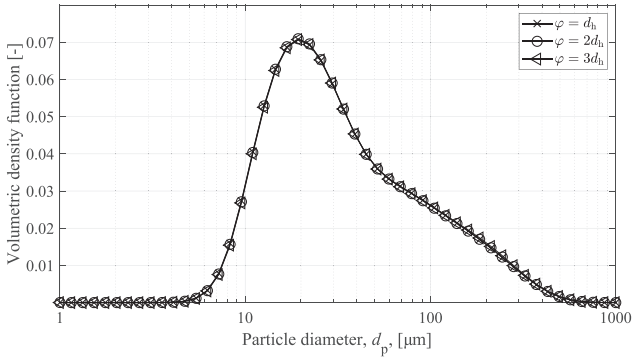

Fig. 3 – Particle size distribution for the 3 simulations with inclination pitches bounded by $d_h \leq \varphi \leq 3d_h$ as well as $L_1 = 5d_h$, $L_2 = 2d_h$ and $r_b = 2d_h$. The difference between the three simulations is negligible.

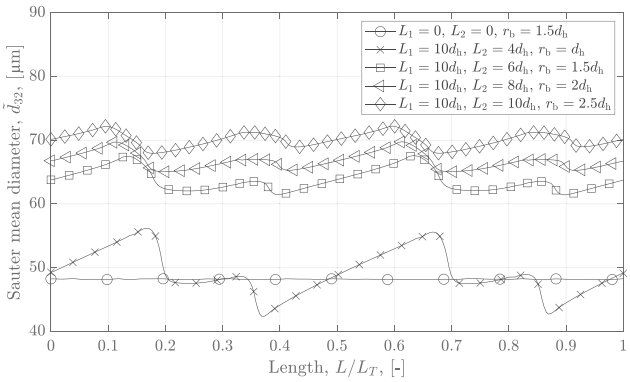

Fig. 4 – Area-averaged Sauter mean diameter, $\tilde{d}_{32}$, as a function of the relative length of the geometrical configuration for 5 different configurations. The mean particle diameter is symmetric around $L/L_T = 0.5$. The self-repeating mean particle diameter is observed for all cases.

configuration with $L_1 = L_2 = 0$, where a constant particle diameter is observed. A constant particle diameter, $\tilde{d}_{32}$, is observed for all cases with no straight pipe lengths, as a constant turbulent energy dissipation rate is observed in these cases.

Between the start of the configuration, $L/L_T = 0$ and the first bend, a linearly increasing trend is observed. When the flow is exposed to the first bend the mean diameter, $\tilde{d}_{32}$, decreases from its peak value to a lower value. As the flow passes the first bend, a linearly increasing Sauter mean diameter is observed as particles have time to aggregate in the low-shear region. As the second bend is encountered, the mean diameter drops once again and if the secondary length is sufficiently short, $L_2 \leq 6d_h$, the Sauter mean diameter drops to a smaller value compared to the first bend. This is observed for all cases, except for the configurations with $L_1 = L_2 = 0$, where the flow is subject to a constant curvature and the turbulent dissipation rate, ε, is therefore kept to a constant magnitude, resulting in a constant mean diameter over the length of the configuration.

4.4. *Local aggregation and breakage*

Analysing the area-averaged Sauter mean diameter in Fig. 4, it is visible that aggregates are more prone to breakage throughout- and downstream of the 90° bend. Calculating the gradient of the mass flow of each size class, $\dot{m}_i$, throughout the length of the configurations using Eq. (24), it is visible what particle size range is affected by the given curvature and velocity profile at the inlet of the bend. This can be applied for each configuration, but the configuration with the smallest radius yields the largest curvature and hence introduces the most turbulence. The configurations with a primary lengths of $L_1 = 10d_h$ and secondary lengths of $4d_h < L_2 < 10d_h$ and a bend radius of $r_b = d_h$ are analysed. This is also the configuration used in Fig. 4. The configurations are analysed at the inlet of the first bend, $\theta = 0°$, halfway through the first bend, $\theta = 45°$, at the outlet of the first bend, $\theta = 90°$ and halfway through the configuration, $L/L_T = 0.5$. The corresponding mass flow into a cell layer, j, is calculated for the given size group, i, as

$$\dot{m}_{i,j} = f_{i,j}\rho_p \, \boldsymbol{u}_{p,j} \cdot \boldsymbol{n}_j A, \tag{23}$$

where $\boldsymbol{n}$ is the normal direction of the face of the computational cell and A is the area of the computational cell.

The mass flow gradient is found by

$$\nabla \dot{m}_{i,j} = \frac{d}{dL}(\dot{m}_{i,j} - \dot{m}_{i,j-1}) \tag{24}$$

The mass flow gradient for the different particle size groups is seen in Fig. 5. When the flow enters the first bend (Fig. 5a) it is visible how medium to large aggregates, $10\,\mu m < d_p < 300\,\mu m$, are formed at a high rate, resulting in a positive production of these aggregates. This is due to a slightly larger turbulent dissipation rate being present at this location. At an angle of 45° through the first bend (Fig. 5b) the turbulent dissipation rate increases to a magnitude where aggregates with a diameter of $d_p > 60\mu m$ breaks at a higher rate than they form, resulting in a negative production of the largest aggregates. This observation is also visible when inspecting the mass flow gradient at the outlet of the bend in Fig. 5c, where it is visible that a positive production of medium-sized aggregates takes place while a negative production of large aggregates is occurring due to the induced turbulence by the curvature of the bend. Halfway through the domain, shown in Fig. 5d, it is visible that larger aggregates, $d_p > 100\mu m$, are formed at a lower rate due to a sufficiently low turbulent dissipation rate, which is supported by the linearly increasing trend observed in Fig. 4 for the straight pipe sections.

This approach provides an in-depth insight into which aggregate sizes form at any given location throughout the configurations and the same tendency is observed for the different bend radii. The magnitude of the mass flow gradient is, however, a function of the bend radius and the inlet velocity profile to a bend, which causes this value to change for the different configurations Fig. 6.

4.5. *Downstream effect of a pipe bend*

It is clear when analysing both Figs. 4 and 5 that the particle diameter decreases over the pipe bend and as the aggregates move downstream from the bend, they start to increase in size again. The gradient of the area-averaged Sauter mean diameter is evaluated along the length of the pipe downstream a bend, $d\,\tilde{d}_{32}/dL$, for the configurations with $L_1 = 10d_h$.

Analysing the gradient of the Sauter mean diameter it is immediately visible how the configurations experience the largest negative gradient immediately at the outlet of a bend, where the configuration with the smallest bend radius, $r_b = d_h$ experiences the largest magnitude when comparing the

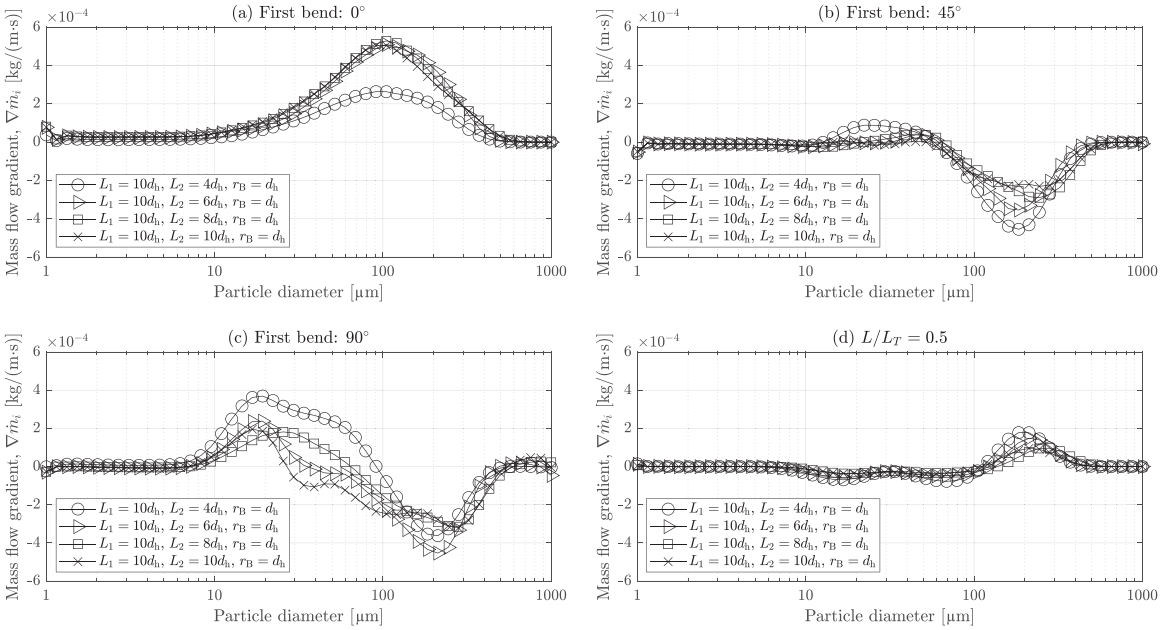

Fig. 5 – Mass flow gradient of the size classes before the first bend, 5a, at an angle of 45° through the first bend, 5b, at the outlet of the first bend, 5c and halfway through the configurations, 5d. A negative mass flow gradient means that the total mass of the size class decreases and the opposite when a positive gradient is observed.

configurations. It is found that the particle size for all configurations starts to recover at a downstream distance of $L > d_h$ from a bend, as a positive gradient is observed for all configurations. When the aggregates start to approach the second bend, the gradient starts to increase, as the turbulent energy dissipation rate increases slightly. This is true except for the configuration with the smallest bend radius, as turbulence is induced over a short length and a negative gradient is observed when approaching the next bend.

For the configurations with the smallest bend radius, $r_b = d_h$, the gradient approaches a constant value after a length of $L = 2d_h$ which means that the particles will aggregate at a constant rate within this length of the pipe. For the configurations with the largest bend radii, $r_b = 2d_h$ and $r_b = 2.5d_h$, the gradient continuously increases after the downstream of the bend. As these configurations experience a less negative gradient at the outlet of the bend and an increasing gradient along the length downstream of the pipe, this explains why these configurations will have the largest overall size when analysing the particle size over the entire domain.

4.6. *Effect of the geometrical configurations*

The Sauter mean diameter is volume-averaged over the entire domain, $\bar{d}_{32}$, to evaluate the geometrical configurations in a single point and thereby compare the different configurations. It is observed that the volume-averaged Sauter mean diameter, $\bar{d}_{32}$, can be categorised based on the bend radius, which is seen in Fig. 7.

It becomes clear that the bend radius is the single most important parameter when aggregating particles in a hydraulic pipe flocculator, as seen when analysing the results in Fig. 7. The overall trend of the configurations is that volume-averaged particle diameter increases as the bend radius increases, which is directly observed when comparing the results from the different bend radii in Fig. 7a to d and this is in good agreement with our previous study (Bilde et al., 2022). The difference in size between the configurations with bend radius $r_b = 2d_h$ and $r_b = 2.5d_h$, in Fig. 7c and d, are small compared to the other bend radii. This indicates that the effect of the bend radius stagnates around $r_b = 2d_h$. Secondly, it is observed that the primary length, L_1, is the second-most important parameter when aggregating the particles. When the primary length of the configuration increases, so does the mean particle diameter. For all simulations it is observed that the simulations with $L_1 = 20d_h$ yield the largest particle diameter, $\bar{d}_{32}$. Thirdly, it is observed that the secondary length, L_2, has the smallest impact when aggregating particles. For the cases with a short primary length, $L_1 \leq 5d_h$, the secondary length becomes the primary length, and therefore the particle diameter, $\bar{d}_{32}$, increases as a function of L_2. For the cases with the longest secondary lengths, $L_2 \geq 10d_h$, it is observed that a short secondary length creates larger aggregates depending on the bend radius. For the largest bend radii, it is observed that $L_2 = 0$ results in the largest overall particle diameter.

An interesting observation is made for the configurations with no straight pipe sections, $L_1 = L_2 = 0$, for all bend radii, as these configurations yield a high particle diameter compared to the configurations with the same bend radius. The helically coiled configuration with bend radii of $r_b = 2d_h$ and $r_b = 2.5d_h$, yields larger volume-averaged particle diameters when compared to the other configurations. As there are no straight pipe sections in these configurations, there is no transition from the bend to the straight pipe where the fluid flow will detach and create a downstream circulation zone (Hellström et al., 2013). These findings are in good agreement with the single-phase numerical findings of Oliveira and Teixeira (2018) and Oliveira et al. (2020).

Besides the findings of the configurations with $L_1 = L_2 = 0$, it is observed for all bend radii, that choosing a system with the longest primary length, $L_1 = 20d_h$ and no secondary length, $L_2 = 0$, results in the largest particle mean diameter.

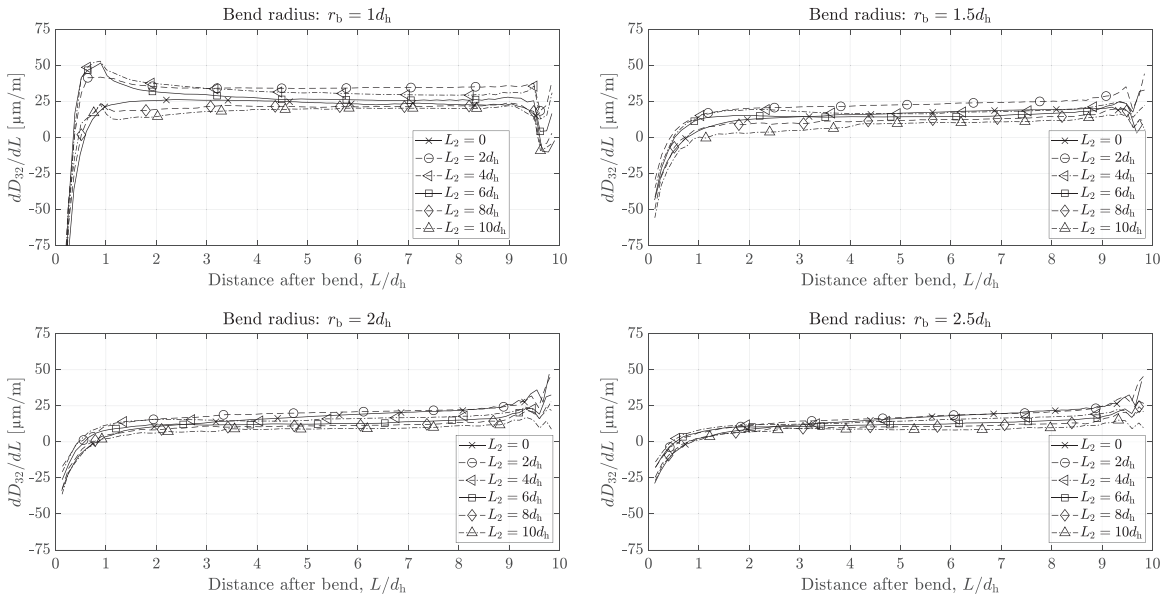

Fig. 6 – Gradient of the Sauter means diameter in the straight section of the pipe for the configurations where $L_1 = 10d_h$. The results are divided into plots according to the bend radius of the configurations, giving 6a: $r_b = d_h$, 6b: $r_b = 1.5d_h$, 6c: $r_b = 2d_h$ and 6d: $r_b = 2.5d_h$.

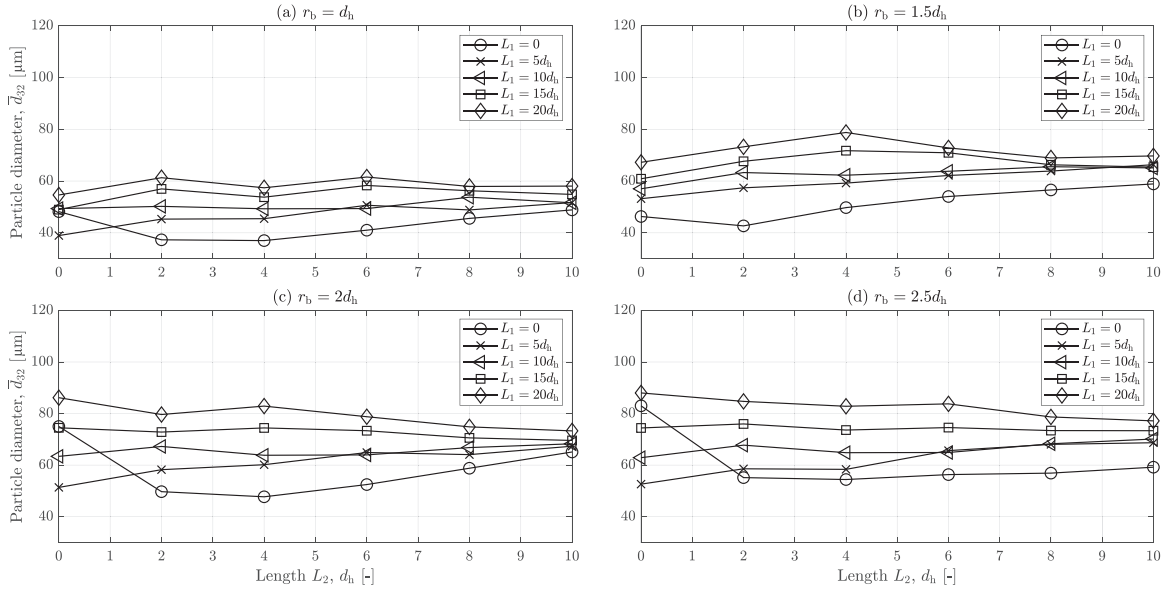

Fig. 7 – Global averaged Sauter mean diameter, $\bar{d}_{32}$, as a function of the secondary length for different primary lengths. 7a: Bend radius of $r_b = d_h$. 7b: Bend radius of $r_b = 1.5d_h$. 7c: Bend radius of $r_b = 2d_h$. 7d: Bend radius of $r_b = 2.5d_h$.

4.7. *Configuration response time*

As all simulations have been started from the same monodisperse particle distribution of $d_p = 1\mu m$, the time to reach a steady-state solution of the given geometrical configuration is of interest. The dimensionless length, $\tilde{L} = t_s u/d_h$, to reach a steady-state solution is used to evaluate the response time of the configurations. The configurations with the lowest induced turbulence produce the largest overall particle size, as seen in Fig. 7, but as a function of this, these systems need the longest time to reach that steady-state solution, which is seen in Fig. 8. The systems with the largest magnitude of induced turbulence, e.g. the systems with the smallest bend radius, produces smaller particles, but the time needed to obtain a steady-state solution is shorter compared to the systems with a larger bend radius.

The response length of the system is generally classified by the bend radius, as a smaller bend radius generally results in a shorter system response length. The configurations with no primary- or secondary lengths, $L_1 = L_2 = 0$, have a longer response time compared to the other configurations with the same bend radius. This is explained by these configurations generally producing larger particles compared to the other configurations with the same bend radius and a longer response length is thereby needed. The difference in the dimensionless length needed to obtain a steady-state solution for the two largest bend radii, $r_b = 2d_h$ and $r_b = 2.5d_h$, there is only needed a slightly longer configuration to achieve a steady-state solution. As the particle size from the configurations is within a similar range, this is also expected.

The response time for a configuration is highly dependent on the initial particle size, as the system will go towards a

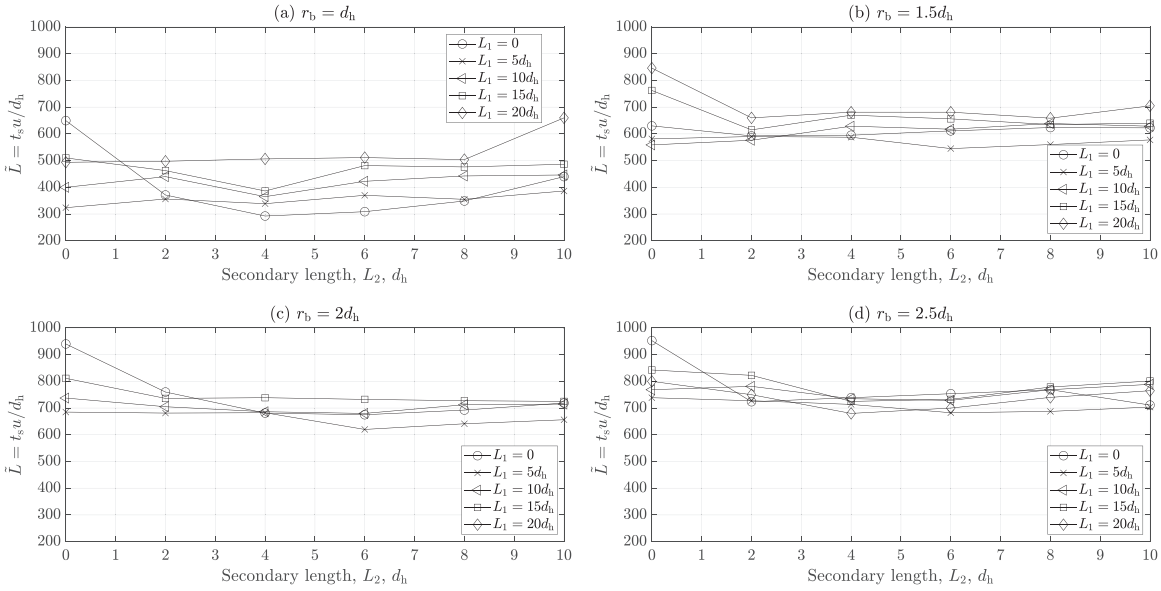

Fig. 8 – The dimensionless length needed to obtain a steady-state solution for the configurations. The dimensionless lengths for $r_b = d_h$ are shown in 8a, the lengths for $r_b = 1.5d_h$ are shown in 8b, the lengths for $r_b = 2d_h$ are shown in 8c and the lengths for $r_b = 2.5d_h$ are shown in 8d.

steady-state solution. In this study, where the simulation is initialised with monodisperse particles of $d_p = 1\mu m$, the particles need to aggregate until a steady-state solution. The opposite initialisation could also be imagined, where the simulation is initialised with monodisperse particles of $d_p = 1000\mu m$ and the particles would then converge towards a steady-state solution by breakage instead of aggregation. This would result in a different response time for the configurations.

5. Conclusion

A numerical multiphase model is applied to simulate the aggregation and breakage of micron-sized particles subject to a turbulent fluid flow with a Reynolds number of $Re = 20,000$. The fluid-particle flow is modelled using the multi-fluid model where the particle number density function is modelled using the population balance equation that is solved using the class method implemented into the open-source CFD library OpenFOAM. The interfacial forces between the solid- and liquid phases are modelled using external force models. Monodisperse particles are inserted into a fully developed fluid velocity profile to initialise the simulation and track the time to reach a steady-state solution for the particle size distribution.

The geometrical parameters of a compact pipe flocculator are varied by changing the primary length, L_1, the secondary length, L_2, the bend radius r_b and the pitch of inclination, φ. The primary length is bounded by $0 \leq L_1 \leq 20d_h$, the secondary length is bounded by $0 \leq L_2 \leq 10d_h$ and the bend radius is bounded by $d_h \leq r_b \leq 2.5d_h$. A total of 123 simulations are completed to analyse the impact of the geometrical configurations under the turbulent flow conditions. It is found that the pitch of inclination has a negligible impact on the particle size distribution, which has the practical meaning that pipe flocculators can be made compact in the vertical direction without loss of performance.

Analysing the impact of the other geometrical parameters shows that the bend radius has the most significant impact on the particle size, as a smaller bend radius induces more turbulence due to the increased curvature in the bend. As the break-up of the aggregates is driven by turbulence, this causes the aggregates to break up at an increased rate compared to configurations with a larger bend radius.

Helically coiled configurations with no straight pipes, $L_1 = L_2 = 0$, and bend radius of $r_b \geq 2d_h$, resulted systems yielding large aggregates compared to other configurations with the same bend radius. This is explained by the lack of a re-circulation zone downstream from the pipe bend, which significantly increases the turbulence induced downstream of the pipe. These configurations comes at the cost of the longest dimensionless length needed to obtain a steady-state solution when initialising with monodisperse particles of $d_p = 1\mu m$.

This study highlights the challenges of designing a compact hydraulic pipe flocculator as the available space often dictates the best configuration. The configurations simulated have a small- to medium footprint and therefore rely on the available height. It is shown that the configuration with a primary length of $L_1 = 20d_h$, a secondary length of $L_2 = 0$ and a bend radius of $r_b = 2.5d_h$ results in the largest volume-averaged particle diameter for $Re = 20,000$ and particle properties resembling soot particles.

In practical terms, this means that the design of a compact hydraulic flocculator becomes long and narrow with fewer connections to weld, which makes manufacturing and installation easier for industries where the available footprint is small but the available height is large.

Declaration of Competing Interest

The authors declare that they have no known competing financial interests or personal relationships that could have appeared to influence the work reported in this paper.

Acknowledgements

This work is financially supported by the Innovation Fund Denmark under grant no. 9065–00188B. The authors

acknowledge Anders Schou Simonsen for his valuable input during this work.

References

Adachi, Y., Cohen Stuart, M.A., Fokkink, R., 1994. Kinetics of turbulent coagulation studied by means of end-over-end rotation. J. Colloid Interface Sci. 165, 310–317. https://doi.org/10.1006/JCIS.1994.1234

Bilde, K.G., Hærvig, J., Lehnigk, R., Schlegel, F., Sørensen, K., 2022. On the agglomeration and breakage of particles in turbulent flows through pipe bends using CFD-PBE. Chem. Eng. Sci. 260, 117915. https://doi.org/10.1016/J.CES.2022.117915

Bridgeman, J., Jefferson, B., Parsons, S., 2008. Assessing floc strength using CFD to improve organics removal. Chem. Eng. Res. Des. 86, 941–950. https://doi.org/10.1016/J.CHERD.2008.02.007

Bridgeman, J., Jefferson, B., Parsons, S.A., 2010. The development and application of CFD models for water treatment flocculators. Adv. Eng. Softw. 41, 99–109. https://doi.org/10.1016/J.ADVENGSOFT.2008.12.007

Bridgeman, J.M., 2006, Investigating the relationship between shear and floc fate using CFD. Ph.D. thesis. Cranfield University.

Burns, A.D., Frank, T., Hamill, I., Shi, J.M., 2004, The Favre averaged drag model for turbulent dispersion in Eulerian multiphase flows.5th International Conference on Multiphase Flow, 1–17.

Camp, T.R., Stein, P.C., 1943. Velocity gradients and internal work in fluid motion. J. Boston Soc. Civ. Eng. 30, 219–237.

Escue, A., Cui, J., 2010. Comparison of turbulence models in simulating swirling pipe flows. Appl. Math. Model. 34, 2840–2849. https://doi.org/10.1016/J.APM.2009.12.018

Fan, M., Chen, L., Li, S., Zou, M., Su, L., Tao, J., 2016. The effects of morphology and water coating on the optical properties of soot aggregates. Aerosol Air Qual. Res. 16, 1315–1326. https://doi.org/10.4209/aaqr.2015.04.0250

Gar Alalm, M., Nasr, M., Ookawara, S., 2016. Assessment of a novel spiral hydraulic flocculation/sedimentation system by CFD simulation, fuzzy inference system, and response surface methodology. Sep. Purif. Technol. 169, 137–150. https://doi.org/10.1016/J.SEPPUR.2016.06.019

Hellström, L.H., Zlatinov, M.B., Cao, G., Smits, A.J., 2013. Turbulent pipe flow downstream of a 90° bend. J. Fluid Mech. 735, R7. https://doi.org/10.1017/jfm.2013.534

Jeldres, R.I., Fawell, P.D., Florio, B.J., 2017. Population balance modelling to describe the particle aggregation process: A review. Powder Technol. 326, 190–207. https://doi.org/10.1016/j.powtec.2017.12.033

Jiang, Z., Rai, K., Tsuji, T., Washino, K., Tanaka, T., Oshitani, J., 2020. Upscaled DEM-CFD model for vibrated fluidized bed based on particle-scale similarities. Adv. Powder Technol. 31, 4598–4618. https://doi.org/10.1016/j.apt.2020.10.009

Kumar, S., Ramkrishna, D., 1996. On the solution of population balance equations by discretization—I. A fixed pivot technique. Chem. Eng. Sci. 51, 1311–1332. https://doi.org/10.1016/0009-2509(96)88489-2

Kusters, K.A., 1991, The influence of turbulence on aggregation of small particles in agitated vessels. Ph.D. thesis. Technische Universiteit Eindhoven.10.6100/IR362582.

Laakkonen, M., Moilanen, P., Alopaeus, V., Aittamaa, J., 2007. Modelling local bubble size distributions in agitated vessels. Chem. Eng. Sci. 62, 721–740. https://doi.org/10.1016/J.CES.2006.10.006

Laine, S., Phan, L., Pellarin, P., Robert, P., 1999. Operating diagnostics on a flocculator-settling tank using fluent CFD software. WIT Trans. Ecol. Environ. 33. https://doi.org/10.2495/WP990251

Lau, P., Kind, M., 2016. CFD-PBE simulation to predict particle growth in a fluidized bed melt granulation batch process. Powder Technol. 300, 28–36. https://doi.org/10.1016/J.POWTEC.2016.02.040

Lehnigk, R., Bainbridge, W., Liao, Y., Lucas, D., Niemi, T., Peltola, J., Schlegel, F., 2021. An open-source population balance modeling framework for the simulation of polydisperse multiphase flows. AIChE J., e17539. https://doi.org/10.1002/AIC.17539

Li, D., Gao, Z., Buffo, A., Podgorska, W., Marchisio, D.L., 2017. Droplet breakage and coalescence in liquid-liquid dispersions: Comparison of different kernels with EQMOM and QMOM. AIChE J. 63, 2293–2311. https://doi.org/10.1002/AIC.15557

Liao, Y., Oertel, R., Kriebitzsch, S., Schlegel, F., Lucas, D., 2018. A discrete population balance equation for binary breakage. Int. J. Numer. Methods Fluids 87, 202–215. https://doi.org/10.1002/FLD.4491

Mandelbrot, B.B., 1985. Self-affine fractals and fractal dimension. Phys. Scr. 32, 257. https://doi.org/10.1088/0031-8949/32/4/001

Marchisio, D.L., Vigil, R.D., Fox, R.O., 2003. Implementation of the quadrature method of moments in CFD codes for aggregation - breakage problems. Chem. Eng. Sci. 58, 3337–3351. https://doi.org/10.1016/S0009-2509(03)00211-2

Mei, R., 1992. An approximate expression for the shear lift force on a spherical particle at finite reynolds number. Int. J. Multiph. Flow. 18, 145–147. https://doi.org/10.1016/0301-9322(92)90012-6

Mikhailov, E.F., Vlasenko, S.S., Podgorny, I.A., Ramanathan, V., Corrigan, C.E., 2006. Optical properties of soot-water drop agglomerates: An experimental study. J. Geophys. Res.: Atmospheres 111, 7209. https://doi.org/10.1029/2005JD006389

Oliveira, D.S., Teixeira, E.C., 2018. Swirl number in helically coiled tube flocculators: theoretical, experimental, and CFD modeling analysis. Int. J. Environ. Sci. Technol. 16, 3735–3744. https://doi.org/10.1007/s13762-018-2027-x

Oliveira, D.S., Teixeira, E.C., Donadel, C.B., 2020. Novel approaches for predicting efficiency in helically coiled tube flocculators using regression models and artificial neural networks. Water Environ. J. 34, 550–562. https://doi.org/10.1111/WEJ.12484

Oliveira, D.S. d., Donadel, C.B., 2019. Global velocity gradient evaluation: An innovative approach using CFD modeling applied to water and wastewater treatment plants. J. Water Process Eng. 28, 21–27. https://doi.org/10.1016/J.JWPE.2018.12.009

Passalacqua, A., Laurent, F., Madadi-Kandjani, E., Heylmun, J.C., Fox, R.O., 2018. An open-source quadrature-based population balance solver for OpenFOAM. Chem. Eng. Sci. 176, 306–318. https://doi.org/10.1016/J.CES.2017.10.043

Qiu, L.C., Liu, J.J., Liu, Y., Lin, P.Z., Han, Y., 2016, CFD-DEM Simulation of Flocculation and Sedimentation of Cohesive Fine Particles, in: Proceedings of the 7th International Conference on Discrete Element Methods, 537–542.10.1007/978–981-10–1926-5_55.

Saffman, P., 1965. The lift on a small sphere in a slow shear flow. J. Fluid Mechanics1 22, 385–400. https://doi.org/10.1017/S0022112065000824

Salehi, F., Cleary, M.J., Masri, A.R., 2017. Population balance equation for turbulent polydispersed inertial droplets and particles. J. Fluid Mech. 831, 719–742.

Sartori, M., Oliveira, D.S., Teixeira, E.C., Rauen, W.B., Reis, N.C., 2015. CFD modelling of helically coiled tube flocculators for velocity gradient assessment. J. Braz. Soc. Mech. Sci. Eng. 37, 187–198. https://doi.org/10.1007/s40430-014-0141-3

Smoluchowski, M. v., 1917. Versuch einer mathematischen Theorie der Koagulationskinetik kolloider Lösungen. Z. für Phys. Chem. 92, 129–168. https://doi.org/10.1515/ZPCH-1918-9209

Tausendschön, J., Kolehmainen, J., Sundaresan, S., Radl, S., 2020. Coarse graining Euler-Lagrange simulations of cohesive particle fluidization. Powder Technol. 364, 167–182. https://doi.org/10.1016/j.powtec.2020.01.056

Törnblom, O., 2018. Turbulent Shear and Breakup of Flocculated Biomaterial in Centrifuge Inlets. Chem. Eng. Technol. 41, 2366–2374. https://doi.org/10.1002/ceat.201800297

Vadasarukkai, Y.S., Gagnon, G.A., Campbell, D.R., Clark, S.C., 2011. Assessment of hydraulic flocculation processes using

CFD. Am. Water Works Assoc. 103, 66–80. https://doi.org/10.1002/j.1551-8833.2011.tb11567.x

Wang, P., Shen, S., Zhou, L., Liu, D., 2019. Turbulent Aggregation and Deposition Mechanism of Respirable Dust Pollutants under Wet Dedusting using a Two-Fluid Model with the Population Balance Method. Int. J. Environ. Res. Public Health 16. https://doi.org/10.3390/ijerph16183359

Wang, X., Cui, B., Wei, D., Song, Z., He, Y., Bayly, A.E., 2022. CFD-PBM modelling of tailings flocculation in a lab-scale gravity thickener. Powder Technol. 396, 139–151. https://doi.org/10.1016/J.POWTEC.2021.10.054

Wen, C., Yu, Y., 1966. Mechanics of Fluidization. Chem. Eng. Prog. Symp. . Ser. 162, 100–111.

Xiang, P., Wan, Y., Wang, X., Lian, H., 2018. Numerical simulation and experimental study of electrocoagulation grid flocculation tank. Water Sci. Technol. 78, 786–794. https://doi.org/10.2166/wst.2018.348

Yakhot, V., Orszag, S.A., Thangam, S., Gatski, T.B., Speziale, C.G., 1992. Development of turbulence models for shear flows by a double expansion technique. Phys. Fluids A 4, 1510–1520. https://doi.org/10.1063/1.858424

Yao, Y., He, Y.J., Luo, Z.H., Shi, L., 2014a. 3D CFD-PBM modeling of the gas-solid flow field in a polydisperse polymerization FBR: The effect of drag model. Adv. Powder Technol. 25, 1474–1482. https://doi.org/10.1016/J.APT.2014.04.001

Yao, Y., Su, J.W., Luo, Z.H., 2014b. CFD-PBM modeling polydisperse polymerization FBRs with simultaneous particle growth and aggregation: The effect of the method of moments. Powder Technol. 272, 142–152. https://doi.org/10.1016/j.powtec.2014.11.037

Yuan, C., Laurent, F., Fox, R.O., 2012. An extended quadrature method of moments for population balance equations. J. Aerosol Sci. 51, 1–23. https://doi.org/10.1016/J.JAEROSCI.2012.04.003

Zhan, M., You, M., Liu, L., Zhang, Y., Yuan, F., Guo, B., Cheng, G., Xu, W., 2021. Numerical simulation of mechanical flocculation in water treatment. J. Environ. Chem. Eng. 9, 105536. https://doi.org/10.1016/j.jece.2021.105536